


Excitons in layered BiI₃: Effects of dimensionality and crystal anisotropy

Jorge Cervantes-Villanueva ^{1,*}, Fulvio Paleari ², Alberto García-Cristóbal ¹, Davide Sangalli ³,
and Alejandro Molina-Sánchez ¹

¹*Institute of Materials Science (ICMUV), University of Valencia, Catedrático Beltrán 2, E-46980, Valencia, Spain*

²*Centro S3, CNR-Istituto Nanoscienze, I-41125 Modena, Italy*

³*Istituto di Struttura della Materia-CNR (ISM-CNR), Area della Ricerca di Roma 1, Monterotondo Scalo, Italy*

 (Received 24 October 2023; revised 17 February 2024; accepted 29 February 2024; published 10 April 2024)

We carry out a detailed theoretical study of the electronic and optical properties of bulk and monolayer bismuth triiodide (BiI₃), a layered metal halide, using the *ab initio* GW+BSE scheme with a full spinorial formulation. We discuss in detail the effects due to the change of dimensionality and the role of spin-orbit coupling. Moreover, we compute the exciton dispersion by solving the BSE at finite momentum, also analyzing transverse and longitudinal excitons, and the L-T splitting at $\mathbf{q} \approx \Gamma$. The results provide a reference for future experimental measurements. In addition, the interplay between spin-orbit coupling and large binding energy, together with the role of quantum confinement, confirm that BiI₃ is an interesting material for optoelectronic applications and show that it is a good candidate for the study of exciton dynamics.

DOI: [10.1103/PhysRevB.109.155133](https://doi.org/10.1103/PhysRevB.109.155133)

I. INTRODUCTION

Exciton physics is a fascinating topic of research in condensed matter, displaying phenomena such as Bose Einstein condensation (BEC), [1,2] topological nonequilibrium phases [3], BEC-Bardeen Cooper Schrieffer (BCS) crossover [4], the exciton-Mott transition [5], with especially remarkable properties in the realm of two-dimensional (2D) materials [6]. The experimental investigation found an ideal playground in 2D materials [7], such as transition metal dichalcogenides (TMDs), which present large excitonic binding energies of around 500 meV [8]. The large binding energy and the optical band gap in the visible range make TMDs promising materials for optoelectronic device applications, such as electrically driven light emitters, photovoltaic solar cells, photodetectors, and valleytronic devices [9,10]. Recent experiments demonstrate the electrical control of excitons [11] and the properties of exciton complexes [12], along with promising application of 2D materials in solid-state devices to implement spin-based computation schemes or to investigate bosonic interactions [13].

In particular, time-resolved spectroscopy is providing unprecedented understanding of exciton properties and dynamics. Recent experiments using time-resolved angle-resolved photoemission spectroscopy (tr-ARPES) [14] have succeeded in probing exciton dynamics in the femtosecond regime, boosting interest in exciton physics. tr-ARPES has been proven useful to monitor the formation of moiré interlayer excitons in TMD heterobilayers [15,16], the hot electron dynamics in monolayer MoS₂ [17], and direct imaging of excitonic wave functions [18].

The materials suitable for exploring the physics and dynamics of excitons exhibit high excitonic binding energies and

large-area samples. Mechanical exfoliation of layered materials achieves a low number of layers, enhancing the excitonic binding energy via quantum confinement and reduced electronic screening of the excitations [19]. In this context, the layered metal halide bismuth triiodide (BiI₃) is a promising candidate for exploring physics of excitons using experimental techniques like tr-ARPES. Bulk BiI₃ is a semiconductor with strong absorption in the visible range, becoming an important candidate for photovoltaic applications [20,21] and for room-temperature γ -ray detectors [22,23]. Initial experimental studies have shown that the bulk has an exciton binding energy of approximately 180 meV, which is unusually large for bulk materials [24,25].

The BiI₃ band-gap value has also been reported as a function of the number of layers, indicating a large difference between the optical and electronic band gaps [26]. Plates and thin films of BiI₃ have been obtained by different methods, such as hot-wall techniques and thermal evaporation methods [27,28]. Monolayer BiI₃ has recently been grown on graphene but with a lower crystalline quality than other monolayer materials like MoS₂ [26], having not yet been exfoliated; however, according to a recent theoretical work [29], mechanical exfoliation of bulk BiI₃ to fabricate monolayers should be possible as in the paradigmatic 2D semiconductor monolayer MoS₂. In addition, bismuth and iodine have large atomic numbers, and thus BiI₃ is subject to a strong spin-orbit interaction, with potential interest for spin physics in 2D materials [30].

Despite the promising optical properties of bulk BiI₃ and the possibilities of synthesizing monolayers, to our knowledge there are no theoretical or computational studies analyzing the physics of excitons in BiI₃. So far, research has focused on the electronic properties [21], optical properties without including spin-orbit coupling [31], and, more recently, a study on coherent phonons [25]. In this context, a complete study of the excitonic states of bulk and monolayer BiI₃, together with the exciton dispersion, is a highly needed reference

*Corresponding author: jorge.cervantes@uv.es

point. In this work we characterize the excitonic states of bulk and monolayer BiI_3 , the two opposite cases with respect to the magnitude of quantum confinement effects and dielectric screening, considering spin-orbit coupling. We start with a comparative analysis of the electronic structure within the GW approach, which is achieved by projecting the bulk band structure onto the 2D Brillouin zone (BZ) of the monolayer. Then we diagonalize the excitonic Hamiltonian, analyze bright and dark excitons, and compute the optical properties of the material. We also compute the exciton dispersion, carefully analyze the longitudinal-transverse (L-T) splitting of bright excitons, and compare our results with the L-T splitting measured by reflection spectroscopy in the bulk [24].

The paper is organized as follows. In Sec. II we report the computational details of the *ab initio* GW+BSE scheme. In Sec. III we present our results for the electronic and optical properties of bulk and monolayer BiI_3 . The physics of excitons in the two systems is investigated in detail, both at zero momentum $\mathbf{q} = \Gamma$ and by analyzing the excitonic dispersion together with the L-T splitting. In Sec. IV we present the conclusions.

II. THEORY AND COMPUTATIONAL DETAILS

Our theoretical study of the exciton physics in BiI_3 is based on first-principles calculations. The computation of the electronic properties is carried out within the framework of density functional theory (DFT) as implemented in the QUANTUM ESPRESSO package [32–34]. We have employed the Perdew-Burke-Ernzerhof (PBE) exchange-correlation functional [35]. BiI_3 is a layered metal halide with a highly ionic bond between bismuth and iodine atoms within the same layer and weak van der Waals forces between layers. Accordingly, we account for van der Waals interaction with the Tkatchenko-Scheffler model (TS-vdW) [36]. Due to the large atomic number of bismuth and iodine atoms, spin-orbit coupling dominates the electronic properties and therefore fully relativistic norm-conserving pseudopotentials are used from PSEUDO-DOJO [37]. The effect of the semicore electrons is considered including explicitly in valence the $4d$ semicore states for iodine and $5d$ semicore states for bismuth due to their reported importance in the electronic structure calculations [38,39]. In previous computational works, optimized lattice parameters were used, which, however, differ by more than 4% with respect to those extracted from experimental data [25]. In this work an attempt to obtain the optimized lattice parameters has been made. However, it has been found that the difference between using theoretical or experimental lattice parameters implies a non-negligible variation in the optoelectronic properties. For that reason we use the experimental lattice parameters of the bulk [40] for both bulk and monolayer (see Table I) and then optimize the atomic positions. In the case of the monolayer, a 15-Å vacuum thickness is imposed in all calculations to avoid fictitious interactions due to the supercell periodicity. The calculations at the DFT level are carried out with a plane-wave cutoff of 80 Ry and the \mathbf{k} grids reported in Table I following the Monkhorst-Pack method [41] (the same \mathbf{k} grids have been used for the GW and BSE calculations).

TABLE I. Computational parameters for the calculation of the electronic and optical properties of bulk and monolayer BiI_3 assuming spin-orbit coupling. (A complete list of the parameters of interest can be found in the Appendix A 7.)

	Bulk	Monolayer
a	7.52 Å	7.52 Å
c	20.7 Å	
GW bands	300	300
GW dielectric cutoff	7 Ry	7 Ry
Static $\epsilon(\omega = 0)$ bands	200	250
BSE bands	139–152	134–152
\mathbf{k}/\mathbf{q} grid	$8 \times 8 \times 8$	$18 \times 18 \times 1$

The inherent underestimation of the DFT band gap is corrected using the GW method [42,43], while optical and excitonic properties are obtained solving the Bethe-Salpeter equation [44], both in the framework of many-body perturbation theory (MBPT) as implemented in the YAMBO code [45–47]. Quasiparticle corrections of the DFT eigenvalues are introduced in a single-shot GW approach (G_0W_0) [48] using the plasmon-pole approximation for the dynamical dependence of the dielectric function [49]. The dielectric function is calculated in the random phase approximation [50]. A truncated Coulomb potential in a slab geometry is used in the monolayer case. This is necessary to avoid interactions between periodic images, and in such a way it is possible to accelerate the convergence of the GW calculations (BSE calculations as well) with respect to the k points, following a combined method of Monte Carlo integration with an interpolation scheme, as developed by Guandalini *et al.* in Ref. [51]. The number of bands included in the calculation of the dielectric matrix in the GW calculation as well as the dielectric cutoff is reported in Table I. In addition, a terminator is used to speed up the convergence of the electronic Green's function G with respect to the empty states [52]. For study of the optical properties considering excitonic effects, the BSE is solved on top of the G_0W_0 results within the Tamm-Dancoff approximation [44]. The exciton dispersion is calculated by solving the finite-momentum BSE in the transferred momenta \mathbf{q} grid shown in Table I. The number of bands used to build the statically screened kernel of the BSE and the valence and conduction bands involved in the calculation of the excitonic transitions are reported in Table I as well. Due to the anisotropy of the system, both for GW and BSE calculations the average of $\mathbf{E} \perp \hat{c}$ and $\mathbf{E} \parallel \hat{c}$ polarizations is adopted to deal with screening at $\mathbf{q} = \Gamma$, \hat{c} being the stacking direction.

III. RESULTS

A. Electronic properties

The crystalline structure of bulk and monolayer BiI_3 is shown in Fig. 1(a). The bulk crystal structure belongs to the space group $R\bar{3}$ (No. 148) [53] and double-point-group symmetry S_6 . The system is defined by a rhombohedral unit cell made of six iodine atoms and two bismuth atoms, as depicted in Fig. 1(b). This results in a three-layer packing structure characterized by an ABC stacking [54]. On the other side,

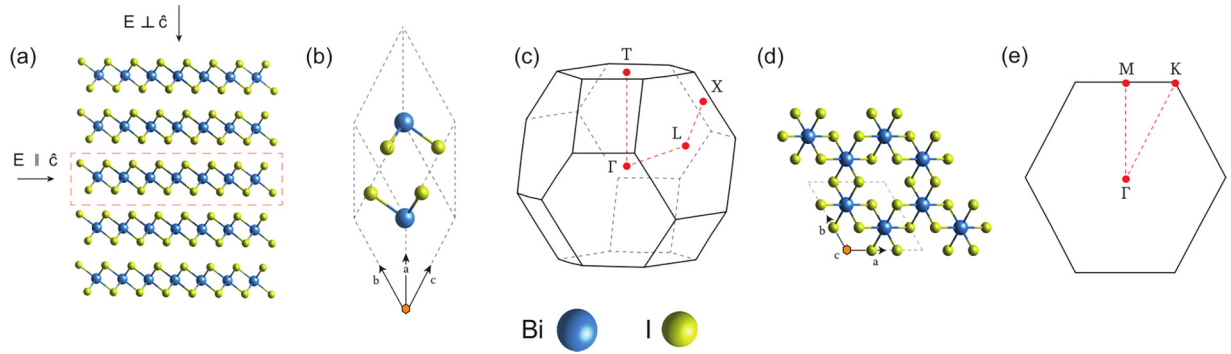


FIG. 1. Crystal structure and Brillouin zone of bulk and monolayer BiI_3 . (a) Side view of bulk BiI_3 , where the dashed box represents the monolayer BiI_3 , (b) unit cell of bulk BiI_3 , (c) Brillouin zone of bulk BiI_3 , (d) unit cell of monolayer BiI_3 , and (e) Brillouin zone of monolayer BiI_3 . In (a), the arrows represent the direction of the incident light. In (b) and (d), the inversion center of the unit cell is highlighted by an orange hexagon.

the crystal structure of the monolayer belongs to the space group $P\bar{3}1m$ (No. 162) [55] and double-point symmetry D_{3d} . The monolayer is determined by a hexagonal unit cell of six bismuth and two iodine atoms, similar to the bulk, Fig. 1(d), with the characteristic hollow of trihalides like CrI_3 [56]. As we will see in the following, this particular stoichiometry brings the structure of this solid closer to that of a molecular crystal with respect to other layered systems, with important consequences on the optical and excitonic properties.

We next analyze the electronic band structure of bulk and monolayer BiI_3 as obtained from calculations at DFT and GW levels. The bulk and monolayer band structures are shown in Figs. 2(a) and 2(b), respectively. The paths in the corresponding BZs are indicated in Figs. 1(c) and 1(e). For clarity, we have selected a simplified path for the bulk case (a more detailed band structure can be found in Appendix A 1). The lowest direct and indirect gaps are indicated by arrows in the corresponding band structures. In both cases the fundamental gap is found to be indirect, which is consistent with the con-

clusions reported previously in the literature [31,57], although the difference with the direct band gap is rather small. To better understand how the change in dimensionality affects the electronic properties, the band structure of monolayer (red lines) and bulk (shaded gray area) BiI_3 are shown together in Fig. 2(c) in the planar hexagonal BZ. Here, the bands of the bulk are integrated over k_z . The region around Γ is the one defining the band gap in both cases. The characteristic off- Γ valence band maxima (VBM) are present both in monolayer and bulk. However, the conduction band minimum (CBM) of the monolayer is located at Γ , whereas in the bulk it is located along the line from Γ to K . This means that, when going from bulk to monolayer, the minimum of the CBM is shifted, slightly changing the wave vector associated to the indirect gap as well as the position of the direct one, analogously to what is observed in TMDs [58,59]. The direct and indirect gaps of the bulk in the hexagonal BZ are marked by arrows.

The calculated band-gap values are reported in Table II. They can be compared with the experimental band-gap values

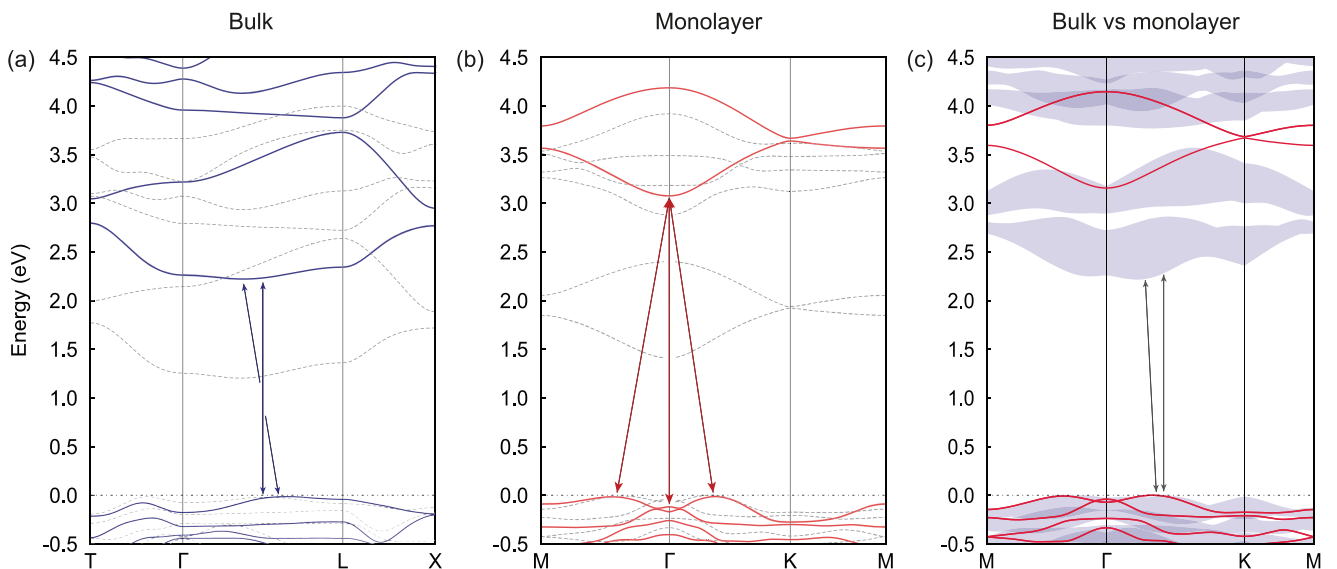


FIG. 2. Electronic band structures of (a) bulk and (b) monolayer BiI_3 considering spin-orbit coupling. The solid lines represent the GW bands, while the dashed ones represent the DFT ones. (c) DFT band structure of bulk (shaded areas) and monolayer (red lines) BiI_3 , both represented in the hexagonal Brillouin zone. The shaded areas represent the integrated dispersion over k_z of the bulk. A scissors operator extracted from the GW calculations is applied to open the gaps.

TABLE II. Band-gap energy values for bulk and monolayer BiI₃ calculated at DFT and GW levels.

	DFT		GW	
	Direct	Indirect	Direct	Indirect
Bulk	1.24	1.19	2.26	2.24
Monolayer	1.45	1.41	3.19	3.09

of 2.65 eV (bulk) and 2.8 (monolayer) measured recently by scanning tunneling spectroscopy [26]. Nevertheless, these experimental values can strongly depend on the sample quality, the presence of substrate, and the fact that a few BiI₃ layers may not correctly represent the bulk properties, resulting in discrepancy with respect to the theoretical values. The difference between the direct and indirect GW band gaps for the bulk is 20 meV (as summarized in Table II), the bulk exhibiting a much flatter conduction band than in the case of the monolayer. This subtle difference between the indirect and direct band gap might be the reason for the discrepancies in the reported values of the fundamental gap and its character (direct or indirect) as extracted from absorption measurements [57]. Our results confirm that the spin-orbit coupling plays a crucial role in describing the electronic properties of this material, since it strongly shifts the CBM down, decreasing the gap value by approximately 1.0 eV (see Appendix A 2, where a comparison is made between the band structures obtained with and without spin-orbit interaction).

In addition, if the 4*d* semicore orbitals for iodine are not included in the DFT+GW calculation, the quasiparticle corrections differ by up to 0.5 eV with respect to the quasiparticle corrections where the 4*d* semicore orbitals are included. For both bulk and monolayer crystals, the quasiparticle corrections significantly modify the valence bands, yet essentially by producing a rigid shift of the conduction bands. In any case, they do not change the nature of the band gaps. The band-gap renormalization due to the quasiparticle corrections is approximately 1.0 and 1.8 eV for bulk and monolayer, respectively. The large difference between bulk and monolayer is linked to quantum confinement effects and to the much weaker dielectric screening in the planar monolayer, which enhances the Coulomb interaction [60]. Moreover, the peculiar crystalline structure of BiI₃, with a hollow site in the lattice formed by bismuth atoms, further reduces the screening and is also responsible for the large band-gap renormalization exhibited by bulk BiI₃.

Concerning other *ab initio* calculations, a direct band-gap value of 2.10 eV was found for the bulk system in a recent work [25] using the GW approach but without including the 4*d* semicore states for iodine atoms and with lattice parameters considerably different from the experimental ones. In the case of the monolayer crystal, a GW direct band gap of 4.20 eV was recently reported in the literature [31]; however, without considering spin-orbit coupling.

B. Exciton physics

The excitonic effects and the optical properties are then computed on top of the quasiparticle band structure. The absorption spectra of the bulk and monolayer BiI₃ for $\mathbf{E} \perp \hat{c}$

and $\mathbf{E} \parallel \hat{c}$ polarizations are shown in Figs. 3(a) and 3(b), where GW+BSE results are compared to the optical absorption without excitonic effects (shaded area), calculated in the independent particle random-phase approximation (IP-RPA). The GW direct-band-gap energy is represented by a vertical dashed line, while the excitonic transitions are represented in the insets below with vertical lines. The yellow lines represent the bright excitons and the blue/red lines the dark excitons. In the bulk case shown in Fig. 3(a), the optical absorption refers to the imaginary part of the macroscopic dielectric function obtained in the calculations, ϵ_2 . In the monolayer case depicted in Fig. 3(b), the imaginary part of the macroscopic dielectric function is not well defined and is more appropriate to work with the polarizability per unit area, $\alpha_{2D}(\omega)$. In order to compare with the bulk case, we define a 2D effective dielectric tensor [61]:

$$\epsilon_{2D}(\omega) = 1 + \frac{4\pi\alpha_{2D}(\omega)}{\Delta z}, \quad (1)$$

with Δz the material thickness in the hexagonal unit cell, being in this case $\Delta z = 7.82 \text{ \AA}$. In both cases the optical response is larger for $\mathbf{E} \perp \hat{c}$ polarization (usually referred to as ordinary geometry) than for $\mathbf{E} \parallel \hat{c}$ (extraordinary geometry). This is especially so in the monolayer, due to the smaller cross-section area. For that reason from now on we will consider the $\mathbf{E} \perp \hat{c}$ case as a reference when necessary.

In the bulk material the first bright exciton transition for $\mathbf{E} \perp \hat{c}$ ($\mathbf{E} \parallel \hat{c}$) is located at 2.12 eV (2.14 eV), therefore indicating an exciton binding energy of 140 meV (120 meV). Experimental measurements on bulk samples reported in the literature [24] indicated an excitonic peak at 2.07 eV (with an exciton binding energy of 180 meV) for $\mathbf{E} \perp \hat{c}$ and at 2.08 eV for $\mathbf{E} \parallel \hat{c}$, both at a temperature of 2 K. Other measurements show that the value of the excitonic peak decreases, when increasing temperature, down to 0.1 eV [62]. Given that neither temperature effects nor the shifts induced by the zero-point motion of ions are considered in our calculations, we consider the theoretical values, although slightly larger, in good agreement with the low-temperature experimental ones.

In the monolayer system the excitonic peak of the first bright exciton for $\mathbf{E} \perp \hat{c}$ ($\mathbf{E} \parallel \hat{c}$) is at 2.30 eV (2.38 eV) with an exciton binding energy of 893 meV (810 meV). The increase of the binding energy compared to the bulk is again due to the enhancement of both the Coulomb interaction (by the change of dielectric environment) and the quantum confinement of electrons, as previously mentioned in the context of the GW calculations. In the previously reported *ab initio* calculations for the monolayer [31], a larger value of 3.18 eV was obtained for the first bright exciton transition for $\mathbf{E} \perp \hat{c}$. The discrepancy with our results is likely due to the neglect of the spin-orbit coupling in Ref. [31].

Remarkably, the values of the exciton binding energies are larger than those of most TMDs. Indeed, for the bulk case [63] only MoTe₂ has a similar binding energy of 150–160 meV [64,65]. The exciton binding energies of the BiI₃ monolayer are much larger than those of the TMDs monolayers, which range between 420 meV for WTe₂ up to 550 meV for the paradigmatic MoS₂ [8,66]. This makes BiI₃ both a good candidate for exciton-based devices and as a playground to study exciton dynamics at room temperature. For instance,

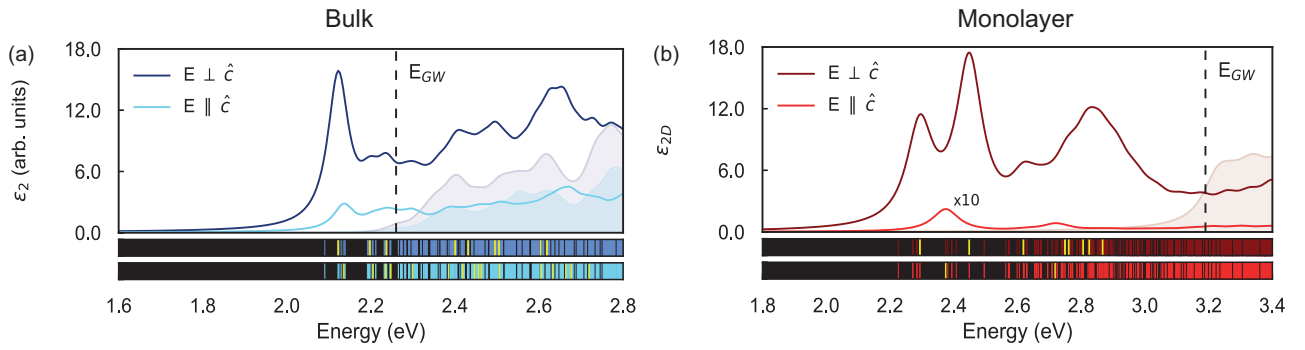


FIG. 3. Absorption spectra for (a) bulk and (b) monolayer BiI₃ assuming spin-orbit coupling obtained with the IP-RPA (shaded areas) and BSE (solid lines) for $\mathbf{E} \perp \hat{c}$ and $\mathbf{E} \parallel \hat{c}$ polarizations. In the case of the monolayer, the BSE spectrum for the $\mathbf{E} \parallel \hat{c}$ polarization has been multiplied by a factor of 10 to be easily observed. The GW direct band gap is marked with a vertical black dashed line. In the insets below, the yellow vertical lines indicate the bright excitons and the rest the dark excitons.

measurements with tr-ARPES would allow for the study of exciton dynamics even in bulk materials [67].

To gain more insight about the excitons and the origin of the large binding energies, exciton wave functions are shown in real space in Fig. 4. The hole is placed on an iodine atom in both cases, since the electrons are located around it in the VBM. The exciton in the bulk is relatively localized considering that it is a bulk system. The reason for this can be partially traced to the crystal structure of the system. In addition to being a layered material, in BiI₃ the crystalline structure is not completely homogeneous within the layer plane but presents hollow regions that result in a stronger localization of the exciton wave function. This effect is more pronounced in the case of the monolayer, where there is no periodicity along the z axis so the confinement effect is quite large. This translates into a much higher exciton binding energy [68].

C. Exciton dispersion

The indirect nature of the band gap of bulk and monolayer BiI₃ makes it necessary to understand the details of the exciton dispersion as a function of the center-of-mass momentum \mathbf{q} to describe its dynamics and the possibility of phonon-assisted optical transitions. For this purpose we solve the BSE for finite momentum transfer \mathbf{q} within the Brillouin zone. The BSE describes the coupling of an electronic valence-to-conduction transition $i = \{v\mathbf{k} - \mathbf{q} \rightarrow c\mathbf{k}\}$ with a second transition $j = \{v'\mathbf{p} - \mathbf{q} \rightarrow c'\mathbf{p}\}$, and the BSE kernel K has the following structure in momentum space [47]:

$$-iK_{ij}(\mathbf{q}) \equiv [W_{ij}^{\text{st}}(\mathbf{k} - \mathbf{p}) - V_{ij}(\mathbf{q})]. \quad (2)$$

In the above abbreviated expression, the first term is the statically screened electron-hole attraction W^{st} and the second one is the bare electron-hole exchange V . Notice the different momentum dependence of the two terms. Equation (2) can be solved with two forms of the exchange term V , either including or not the long-range contribution $v_{\mathbf{G}}^{\text{c,LR}}(\mathbf{q})$ of the bare Coulomb interaction $v_{\mathbf{G}}^{\text{c}}(\mathbf{q}) = 4\pi/|\mathbf{q} + \mathbf{G}|^2$, here \mathbf{G} being a reciprocal lattice vector. We can thus define the “full range,” $V_{ij}^{\text{FR}}(\mathbf{q}) = \langle i|v^{\text{c}}(\mathbf{q})|j\rangle$, or the “short-range,” $V_{ij}^{\text{SR}}(\mathbf{q}) = \langle i|\bar{v}^{\text{c}}(\mathbf{q})|j\rangle$, where $\bar{v}^{\text{c}}(\mathbf{q}) = v^{\text{c}}(\mathbf{q}) - v_{\mathbf{G}}^{\text{c,LR}}(\mathbf{q})$. The inclusion of the long-range contribution leads to an important qualitative difference in the results, since it determines the splitting

between transverse excitons [TE, obtained when $V^{\text{SR}}(\mathbf{q})$ is used in Eq. (2)] and longitudinal excitons [LE, obtained when the full $V^{\text{FR}}(\mathbf{q})$ is applied] [69], in analogy to the LO-TO

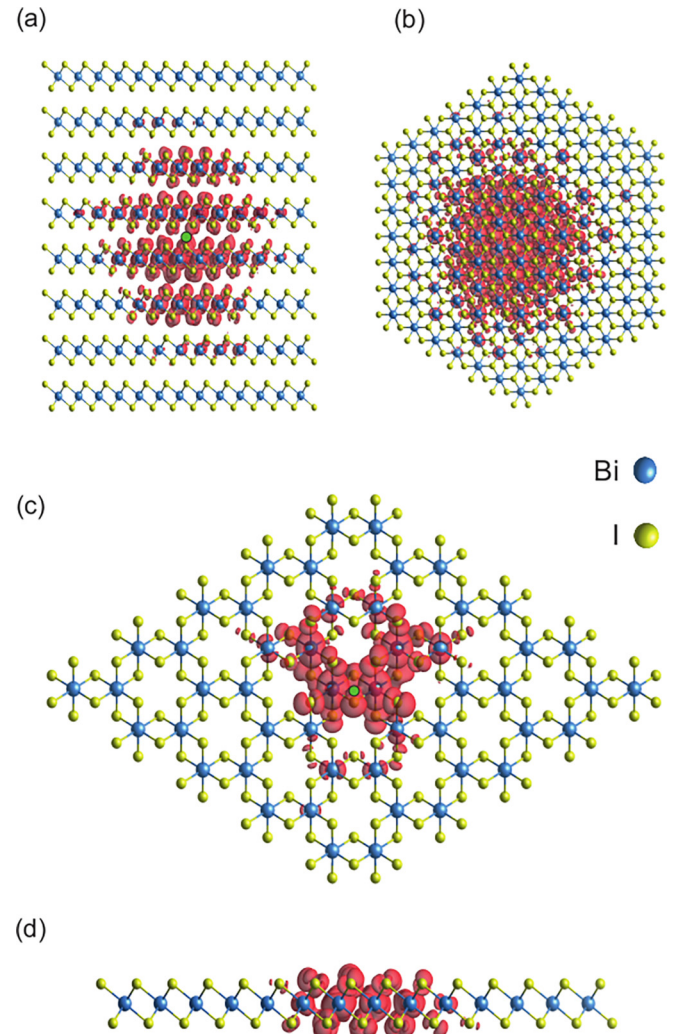


FIG. 4. Exciton wave function of the first bright exciton for $\mathbf{E} \perp \hat{c}$ for (a), (b) bulk and (c), (d) monolayer BiI₃ with spin-orbit coupling. The isosurface value used to depict the exciton wave functions is 15% of the maximum intensity in both cases. The position of the hole is indicated by a green circle.

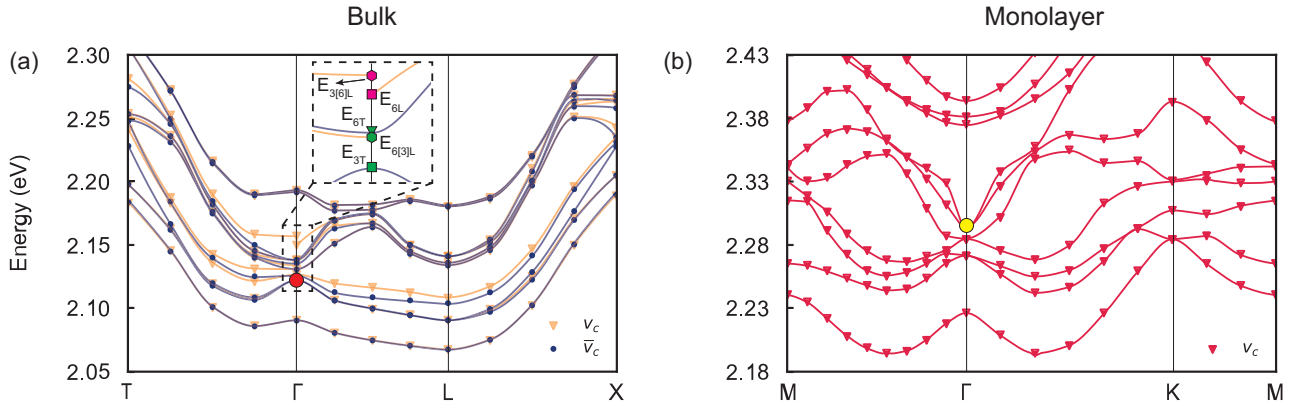


FIG. 5. Exciton dispersion for (a) bulk and (b) monolayer BiI_3 considering spin-orbit coupling. The x axis represents the momentum transfer $\mathbf{q} = \mathbf{k} - \mathbf{k}'$, which coincides with the exciton center-of-mass momentum. Dots are exact calculations, and lines represent interpolated values. The big red and yellow dots indicate the position of the first bright exciton for $\mathbf{E} \perp \hat{c}$ polarization for bulk and monolayer, respectively. The curves labeled with \bar{v}_c (v_c) have been obtained without (with) the inclusion of the long-range exchange electron-hole interaction. In (a), the marks in the inset represent the energies of the optically active excitons for the directions indicated in Fig. 6.

splitting of the optical phonon modes in polar semiconductors [70]; neglecting the long-range contributions nets only the TE energies. The type of L-T splitting can be understood as a manifestation of the anisotropy of the crystal lattice in the excitonic properties. In this case, $v_{\mathbf{G}}^{c,\text{LR}}(\mathbf{q})$ plays a similar role as the long-range dipolar electric field in the phonon case. Indeed, for $\mathbf{q} \rightarrow 0$ [71,72],

$$\langle i | v_{\mathbf{G}}^{c,\text{LR}}(\mathbf{q}) | i \rangle \propto \frac{(\mathbf{q} \cdot \mathbf{d}_i)^* (\mathbf{q} \cdot \mathbf{d}_i)}{q^{p-1}} = |d_i|^2 q^{3-p} \cos^2 \theta, \quad (3)$$

where \mathbf{d}_i is the electric dipole matrix element for the transition i , and θ the relative angle between \mathbf{d}_i (directed along the external electric field) and \mathbf{q} . The presence of the dipoles implies that only optically bright excitons, for which $|\mathbf{d}_i| \neq 0$, can be subject to L-T splitting [73]. Finally, $p = 2, 3$ in 2D and 3D, respectively. This leads to different behaviors in different dimensions [74]. In 3D we have $v_{\mathbf{G}}^{c,\text{LR}}(\mathbf{q}) = v_{\mathbf{G}=0}^c(\mathbf{q}) = 4\pi/|\mathbf{q}|^2$, and there is a finite L-T splitting at $\mathbf{q} = \Gamma$, which depends on the direction along which the limit $\mathbf{q} \rightarrow 0$ is approached. In terms of physical observables, optical absorption—the response of the system to a transverse electromagnetic field—is proportional to the imaginary part of the $\mathbf{q} = 0$ macroscopic transverse dielectric function $\text{Im}\epsilon_T(\omega)$, and $\epsilon_T(\omega) = \epsilon_L(\omega)$ in this limit. Instead, the LE can be observed—also at finite \mathbf{q} —alongside plasmons in electron energy loss spectroscopy (EELS), which is proportional to $\text{Im}\epsilon_L^{-1}(\mathbf{q}, \omega)$. In Fig. 5(a) we show the results of calculations performed using either $V(\mathbf{q}) = V^{\text{FR}}(\mathbf{q})$ or $V(\mathbf{q}) = V^{\text{SR}}(\mathbf{q})$ in Eq. (2). In contrast with the 3D case, in the isolated 2D system the long-range behavior of the exchange interaction emerges from the integration along the z direction of $\langle i | v_{G_x=G_y=0}^c(\mathbf{q}) | j \rangle$ [75]. This results in a term proportional to $|q|$ in the BSE kernel [see Eq. (3)]. Accordingly, at zero momentum there is no effect due to the long-range exchange, e.g., there is no L-T splitting at $q = 0$ in 2D. At finite momentum, because of depolarization effects linked to the effectively infinite \hat{c} axis of the 2D system, $\epsilon_L(\mathbf{q}, \omega)$ and $\epsilon_L^{-1}(\mathbf{q}, \omega)$ capture the same physics at any \mathbf{q} [76], with poles matching the solution of Eq. (2) with the long-range exchange included. For this

reason, in Fig. 5(b) we show only the case in which $V(\mathbf{q}) = V^{\text{FR}}(\mathbf{q})$ [77].

The exciton dispersions of bulk and monolayer BiI_3 are shown in Figs. 5(a) and 5(b) for the first ten excitons. For both systems the minima of the lowest-energy excitons are not located at Γ , which is consistent with having a fundamental indirect gap. We first focus on the bulk, Fig. 5(a), where the excitons are labeled with increasing integers starting from the lowest-energy exciton. Thus, the lowest-energy exciton E_1 exhibits its minimum at $\mathbf{q} = \mathbf{L}$. E_1 is dark and, accordingly, not subject to L-T splitting. E_2 and E_3 are degenerate (red circle) and bright for the $\mathbf{E} \perp \hat{c}$ polarization. Thus, they are subject to L-T splitting, being maximum when the direction of the electric field is in-plane. Finally, E_4 and E_5 are again dark, while E_6 is bright for the $\mathbf{E} \parallel \hat{c}$ polarization. In this case E_6 is nondegenerate, but it is subject to an energy shift, displaying L-T behavior, and the shift being maximum when the direction of the electric field is out-of-plane. The rest of the excitons are dark and therefore not subject to L-T splitting.

To analyze the nonanalytic behavior at $\mathbf{q} = \Gamma$ of the previous excitons, we calculate LE, considering two electric field directions in the limit $\mathbf{q} \rightarrow \mathbf{0}$, e.g., along the directions $\mathbf{T} \rightarrow \Gamma$ and $\mathbf{L} \rightarrow \Gamma$ at $\mathbf{q} = \Gamma$, in line with the exciton dispersion. This is depicted in Fig. 5(a) by the orange lines, where the inset shows the excitons of interest. As expected, an energy shift leading to L-T splitting is only observed in the optically active excitons, which are represented by the green and magenta marks.

The exciton dispersion of the monolayer is depicted in Fig. 5(b) and shows that the lowest-energy exciton has two minima matching the energy indirect transitions of the band structure calculated in Fig. 2(b) (see Appendix A3 for a representation of the excitons on the band structure and in the reciprocal space). In contrast to the bulk, several dark excitons lie below the first bright exciton (yellow circle) for the $\mathbf{E} \perp \hat{c}$ polarization. The linear dispersion can be observed when moving away from $\mathbf{q} = \Gamma$ for the first bright exciton, in agreement with Eq. (3) and what has been reported in previous studies for 2D materials [72,75].

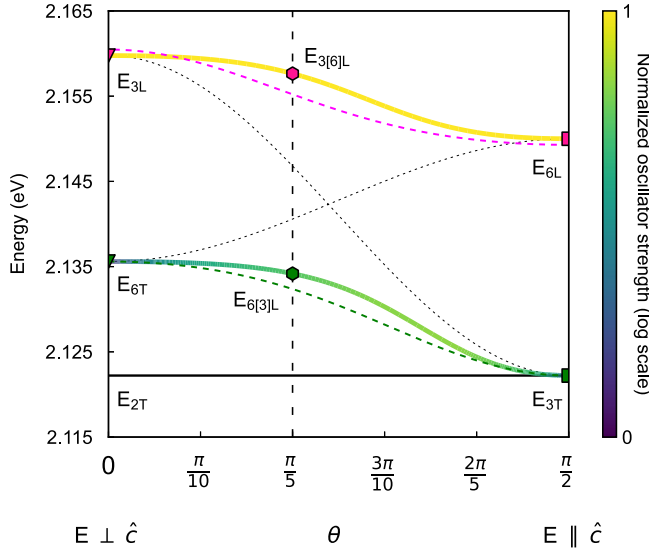


FIG. 6. Behavior of the excitons E_{2-3} and E_6 at $\mathbf{q} = \Gamma$ when the electric field direction changes from $\mathbf{E} \perp \hat{c}$ to $\mathbf{E} \parallel \hat{c}$ as a function of θ , with spin-orbit coupling. The color map represents the normalized oscillator strength, shown on a logarithmic scale. The vertical dashed line defines the angle when the electric field has the direction $T \rightarrow \Gamma$. The horizontal black line represents the energy of the degenerate exciton E_{2T} which is not affected by the change of direction of the electric field. The dotted crossing curves represent the behavior of the LE if they were independent, while the magenta and green dotted curves represent the behavior when they are coupled, according to the two-exciton model in the Appendix A 4. The exciton energies and oscillator strengths have been obtained by solving BSE for 20 different angles and then interpolated to obtain a smooth function.

To perform a more exhaustive analysis of the L-T splitting at $\mathbf{q} = \Gamma$ of bulk BiI₃, Fig. 6 shows the energies of the excitons E_{2-3} and E_6 as a function of the electric field direction. Although the excitons E_{2-3} are degenerate, E_2 is not influenced by the direction change of the electric field while E_3 is affected. We have represented the change from in-plane to the out-of-plane direction as a function of the angle θ , where $\theta = 0$ is in-plane and $\theta = \pi/2$ is out-of-plane direction. One would expect that the two bright states for the in-plane and out-of-plane case exhibit an independent behavior represented by the crossing dashed lines, e.g., the exciton E_3 would experience the maximum splitting when the electric field direction is in-plane, and its energy would decrease to zero when the electric field direction is out-of-plane, due to the direction-dependent decrease in its oscillator strength. The same trend should be exhibited by the energy shift of E_6 . Instead, the two LE show a coupled behavior revealed by the avoided crossing along θ , where one of them has a much lower oscillator strength. This is verified by a two-exciton model, represented in Fig. 6 by the magenta and green dashed lines (see Appendix A 4 for a model description of the independent and coupled cases). In essence, the “transverse” exciton E_{6T} continuously evolves into E_{3T} without losing its transverse (and optically dark) character, while the “longitudinal” split-off exciton E_{3L} becomes the shifted E_{6L} and remains bright for all θ values. The observation of the L-T splitting as a function

TABLE III. Energies of the excitons E_3 and E_6 when the electric field direction changes from $\mathbf{E} \perp \hat{c}$ to $\mathbf{E} \parallel \hat{c}$.

E_{3T}	E_{6T}	E_{6L}	E_{3L}
2.122	2.136	2.150	2.160

of the electric field angle should be possible with EELS or inelastic x-ray scattering (IXS).

As a summary, Table III collects the energies of E_3 and E_6 for the electric field in-plane and out-of-plane directions. We obtain a value of the L-T splitting of 37 meV for the $\mathbf{E} \perp \hat{c}$ polarization, in excellent agreement with the 38 meV measured experimentally [24].

IV. CONCLUSIONS

We have studied the exciton physics of bulk and monolayer BiI₃ with many-body first-principles calculations in the framework of DFT, the GW method, and the Bethe-Salpeter equation. We find that both systems exhibit an indirect fundamental gap. The influence of the dimensionality is evident in the electronic and optical properties. The quasiparticle corrections for the monolayer are much larger than for the bulk, which is consistent with the stronger quantum confinement and the reduction of the dielectric screening. The energies of the first bright excitons for $\mathbf{E} \perp \hat{c}$ and $\mathbf{E} \parallel \hat{c}$ light polarization in bulk are in good agreement with the experimental values. We demonstrate the large exciton binding energies of bulk and monolayer BiI₃, providing a detailed analysis of the excitonic features. The exciton dispersion reaffirms the indirect character of electronic transitions. We find a peculiar direction-dependent hybridization of excitons with different character mediated by the long-range Coulomb interaction embodied in the longitudinal-transverse energy splittings. In addition, our results underscore the importance of a GW+BSE full spinorial description in order to obtain correct quasiparticles and excitons for $\mathbf{q} = 0$ and $\mathbf{q} \neq 0$. Our work provides theoretical support to the existing experiment, demonstrating that BiI₃ is an important testbed for the theoretical study of fundamental exciton physics (such as phonon-mediated exciton interaction and localization), and finally confirms that this system is a promising material for the experimental investigation of exciton dynamics (such as tr-ARPES measurements).

ACKNOWLEDGMENTS

The authors acknowledge the funding of Ministerio de Ciencia e Innovación, which is part of Agencia Estatal de Investigación (AEI), through Project No. PID2020-112507GB-I00 QUANTA-2DMAT (Novel quantum states in heterostructures of 2D materials) and the Generalitat Valenciana through the Grants No. PROMETEO 2021/082 (ENIGMA), No. SEJIGENT 2021/034 (2D-MAGNONICS) and No. MFA 2022/009 (SPINO2D). This study forms part of the Advanced Materials programme and was supported by MCIN with funding from European Union NextGenerationEU (PRTR-C17.I1) and by Generalitat Valenciana. J.C.-V. acknowledges the Contrato Predoctoral Ref. PRE2021-097581. A.M.-S.

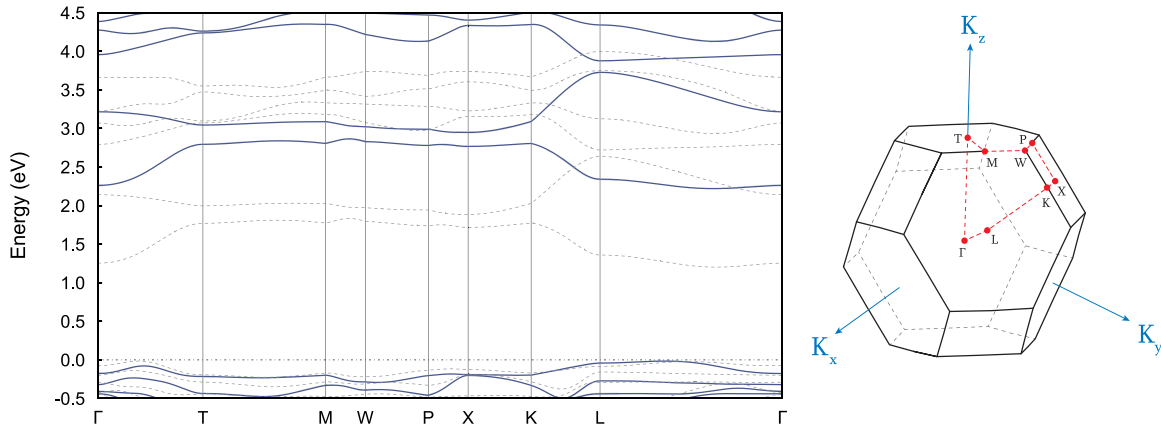


FIG. 7. DFT and GW band structure along the entire path of the Brillouin zone in bulk BiI_3 . The solid lines represent the GW bands, while the dashed ones represent the DFT ones. The inset shows the high-symmetry points in the Brillouin zone.

acknowledges the Ramón y Cajal programme (Grant No. RYC2018-024024-I, MINECO, Spain). This study forms part of the Advanced Materials programme and was supported by MCIN with funding from European Union NextGenerationEU (PRTR-C17.I1) and by Generalitat Valenciana. D.S. and F.P. acknowledge funding from MaX “MAterials design at the eXascale” (Grant Agreement No. 101093374), co-funded by the European High Performance Computing Joint Undertaking (JU) and participating countries. D.S. also acknowledges PRIN Grant No. 20173B72NB funded by MIUR, Italy. F.P. acknowledges P. Cudazzo for useful discussions.

APPENDIX

1. Band structure of bulk BiI_3

The Brillouin zone of bulk BiI_3 has multiple high-symmetry points to consider, as indicated in Fig. 7. However, we have found that not all of these points are relevant in characterizing the important features of the band structure. In order to illustrate the above remark, the band structure of bulk BiI_3 is shown in Fig. 7 along an extended closed path across the Brillouin zone. We see that the valence (conduction) band energies along the T-M-W-P-X path lie below (above) the corresponding band maximum (minimum) and that their dispersion is rather flat in that region. This means that at low energies, that portion of the band structure will not significantly contribute to direct and indirect transitions. For this reason and for the sake of clarity, a simplified path has been used to depict the band structure in Fig. 2(a).

2. Effect of spin-orbit coupling in BiI_3

The importance of considering the spin-orbit coupling in a material can be mainly predicted depending on the atomic number of the constituent atoms. For large atomic numbers, the effect of the spin-orbit coupling on the material properties can be meaningful. In the case of BiI_3 , both the bismuth ($Z = 83$) and iodine ($Z = 53$) atoms are quite heavy, so that the spin-orbit coupling effect is of vital importance. To illustrate this fact, Figs. 8(a) and 8(b) show the DFT band structures for the bulk and monolayer with and without considering

the spin-orbit coupling. In both cases the spin-orbit coupling drastically affects the electronic properties by modifying the shape of the bands and shifting down the CBM by 1.0 eV, thus

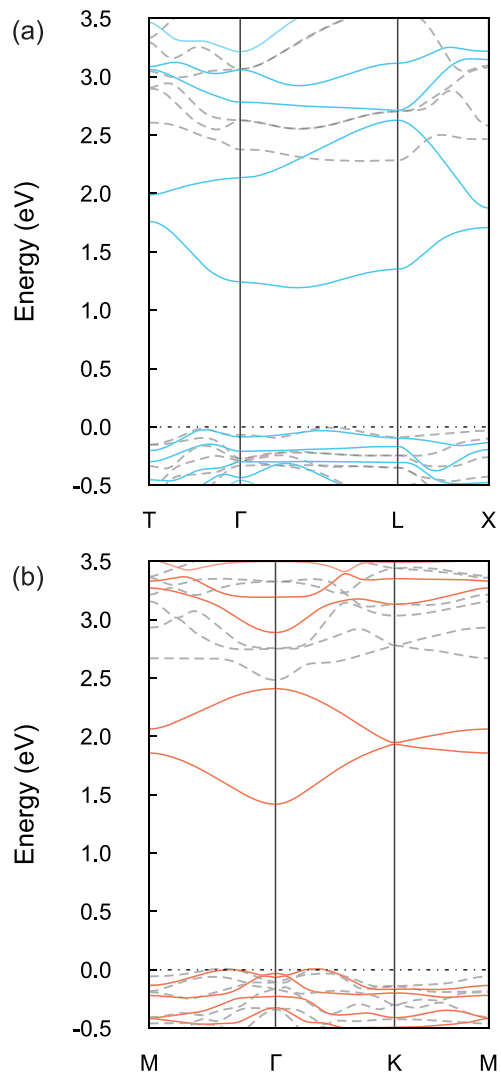


FIG. 8. DFT band structure of (a) bulk and (b) monolayer BiI_3 with (solid lines) and without (dashed lines) spin-orbit coupling.

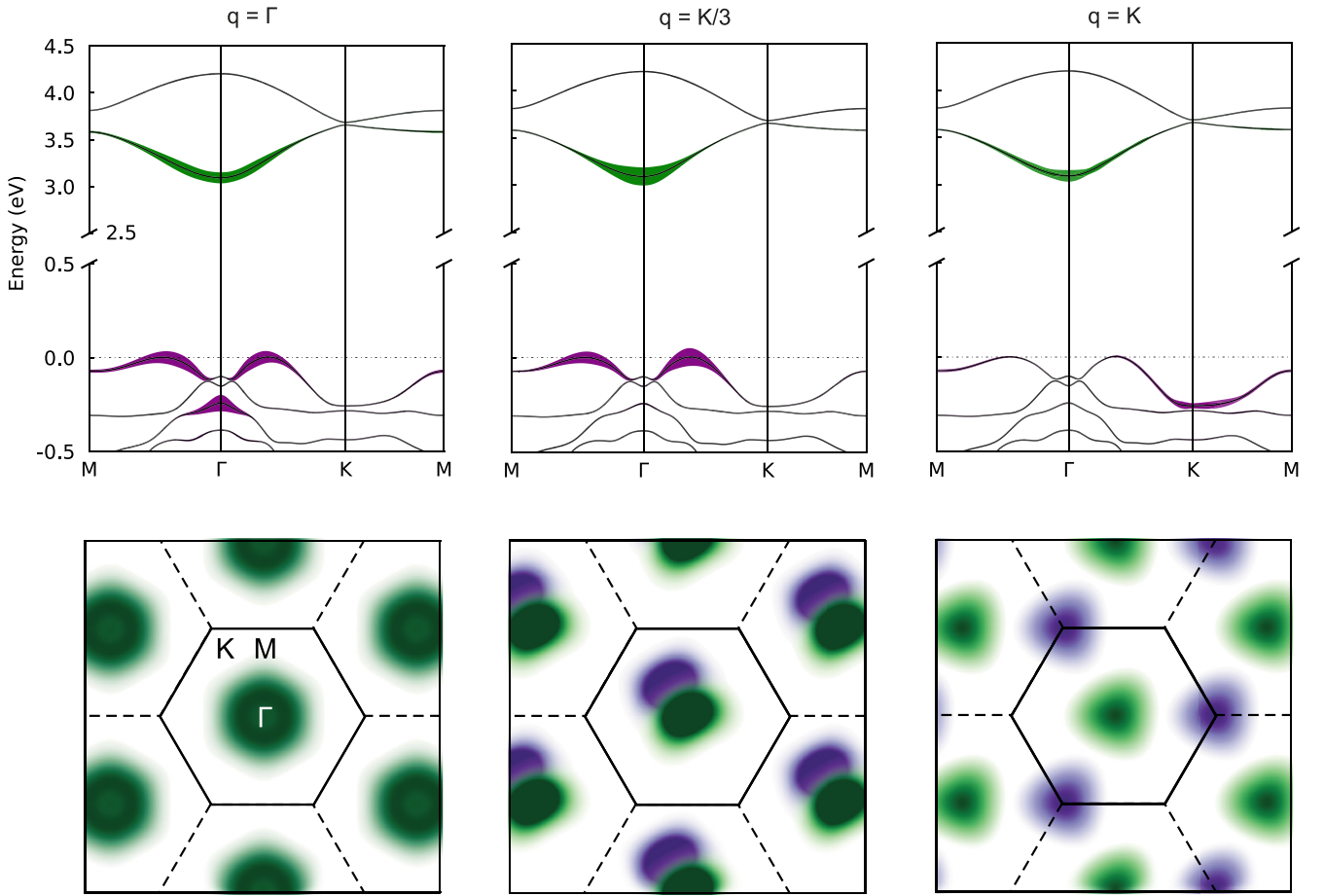


FIG. 9. Representation of the lowest energy exciton, $\lambda = 1$ for different center-of-mass momentum $q = \Gamma, K/3, K$. We plot $F_{v\mathbf{k}-\mathbf{q}}^{\lambda\mathbf{q}}$ and $F_{c\mathbf{k}}^{\lambda\mathbf{q}}$ on the valence and conduction band, and $F_h^{\lambda\mathbf{q}}(\mathbf{k} - \mathbf{q})$ together with $F_e^{\lambda\mathbf{q}}(\mathbf{k})$ in reciprocal space for the monolayer BiI₃. The exciton with center-of-mass momentum $\mathbf{q} = K/3$ corresponds to the minimum of the exciton dispersion (see Fig. 5(b) in the main text), and the same momentum is associated to the lowest energy transition in the band structure.

changing the position of the transitions, decreasing the value of the gap, and finally modifying the optical properties.

3. Representation of excitonic wave functions in reciprocal space

In order to get further insight on the excitonic properties we define the amplitude of the exciton wave function in the Brillouin zone as:

$$F_{v\mathbf{k}-\mathbf{q}}^{\lambda\mathbf{q}} = \sum_c |A_{cv\mathbf{k}}^{\lambda\mathbf{q}}|^2, \quad (\text{A1})$$

$$F_{c\mathbf{k}}^{\lambda\mathbf{q}} = \sum_v |A_{cv\mathbf{k}}^{\lambda\mathbf{q}}|^2, \quad (\text{A2})$$

where $A_{cv\mathbf{k}}^{\lambda\mathbf{q}}$ are the coefficients of the exciton wave function λ of momentum \mathbf{q} in the transition space (see more details in Ref. [45–47]). $F_{v\mathbf{k}-\mathbf{q}}^{\lambda\mathbf{q}}$ and $F_{c\mathbf{k}}^{\lambda\mathbf{q}}$ are the amplitudes in conduction and valence band, respectively. The total amplitude is obtained by summing over all conduction and valence band states, respectively:

$$F_h^{\lambda\mathbf{q}}(\mathbf{k} - \mathbf{q}) = \sum_v F_{v\mathbf{k}-\mathbf{q}}^{\lambda\mathbf{q}} = \sum_{cv} |A_{cv\mathbf{k}}^{\lambda\mathbf{q}}|^2 = \sum_c F_{c\mathbf{k}}^{\lambda\mathbf{q}} = F_e^{\lambda\mathbf{q}}(\mathbf{k}). \quad (\text{A3})$$

In Fig. 9 we have represented the amplitudes of exciton wave functions of lowest energy for $\mathbf{q} = \Gamma, \mathbf{q} = K/3$ and $\mathbf{q} = K$ directions, both in the band structure [Eqs. (A1) and (A2)] and on the 2D BZ [Eq. (A3)] for monolayer BiI₃. The plots demonstrate that the minimum of the exciton dispersion corresponds to the lowest energy (indirect) transition in the band structure. The purple contribution represents the exciton weight in the valence manifold, while the green one represents the weight in the conduction manifold. The exciton with center-of-mass momentum $\mathbf{q} = K/3$ is the minimum of the exciton dispersion and corresponds in fact to the lowest energy indirect transition in the band structure. The representation in the reciprocal space shows where these transitions take place

TABLE IV. Computational parameters for the DFT calculations of bulk and monolayer BiI₃.

	Bulk	Monolayer
a	7.52 Å	7.52 Å
c	20.7 Å	–
Plane-wave cutoff	80 Ry	80 Ry
Number of bands	300	300
\mathbf{k} grid	$8 \times 8 \times 8$	$18 \times 18 \times 1$

TABLE V. Computational parameters for the GW calculations of bulk and monolayer BiI₃.

	Bulk	Monolayer
Plane-wave cutoff	50 Ry	50 Ry
Exchange cutoff	60 Ry	60 Ry
XC potential cutoff	DFT value	DFT value
GW bands	300	300
Dielectric cutoff	7 Ry	7 Ry
k grid	8 × 8 × 8	18 × 18 × 1

within the Brillouin zone. Despite the fact that $F_h^{\lambda\mathbf{q}}(\mathbf{k} - \mathbf{q})$ and $F_e^{\lambda\mathbf{q}}(\mathbf{k})$ contain the same information, representing them together directly gives a visualization of the transferred momentum \mathbf{q} , which is fixed in the plot, and of the relative position of electrons and holes (which is also independent from the convention used in the equations, e.g. $\mathbf{k} - \mathbf{q}$ for the holes).

4. Behavior of L-T splitting as a function of the electric field direction

The avoided-crossing behavior manifested by the two LE states in Fig. 6 is due to the fact that they are coupled, which can be better understood in terms of a simple two-exciton model. In this model we reproduce the behavior of the uncoupled and coupled LE considering explicitly the long-range Coulomb interaction $v_{G=0}^c$. We start defining the short-range excitonic Hamiltonian:

$$H^{\text{SR}} = H^0 + V^{\text{SR}} - W^{\text{st}}, \quad (\text{A4})$$

where H^0 is the quasiparticle energy difference (diagonal in the basis of electronic transitions), V^{SR} is the bare electron-hole exchange without including the long-range contribution, and W^{st} is the statically screened electron-hole attraction (the term responsible for electron-hole binding), already defined in Eq. (2). Then we define the full excitonic Hamiltonian:

$$H = H^{\text{SR}} + V^{\text{LR}}, \quad (\text{A5})$$

with V^{LR} being the long-range exchange contribution (in 3D it originates from the $\mathbf{G} = 0$ term of the Coulomb interaction, e.g., $v_{G=0}^c$, see discussion in the main text). In the excitonic space ($|\alpha\rangle, |\beta\rangle$), being transverse excitonic states which diago-

 TABLE VI. Computational parameters for the BSE calculations of bulk and monolayer BiI₃.

	Bulk	Monolayer
Plane-wave cutoff	50 Ry	50 Ry
Static screening bands	200	250
Static screening cutoff	2 Ry	4 Ry
Exchange BSE kernel cutoff	15 Ry	15 Ry
Direct BSE kernel cutoff	2 Ry	2 Ry
BSE bands	139–152	134–152
k grid	8 × 8 × 8	18 × 18 × 1

nalize H^{SR}), for 3D materials and $\mathbf{q} \rightarrow 0$ it reads

$$\langle \alpha | v^{c,\text{LR}} | \beta \rangle = C \frac{(\mathbf{q} \cdot \mathbf{D}_\alpha^*)(\mathbf{q} \cdot \mathbf{D}_\beta)}{q^2}, \quad (\text{A6})$$

where C is a dimensional constant, \mathbf{q} is the momentum vector, and \mathbf{D}_α is the exciton dipole vector, for exciton α . We call E_{b_α} the eigenvalues of H^{SR} (supposed known from the simulations) and E_α those of H , which are to be determined in the model. Since we are dealing with BiI₃, we define the bright exciton with dipole along x (in-plane) as E_{b_3} and with the dipole along z (out-of-plane) as E_{b_6} . It should be noted that the direction of the excitonic dipoles is also known in advance due to the crystal symmetry.

5. Uncoupled bright excitons

In the case of uncoupled LE the long-range exchange in Eq. (A6) is diagonal and therefore Eq. (A5) gives the following energies:

$$E_3 = E_{b_3} + C|D_2|^2 \cos^2 \theta, \quad (\text{A7})$$

$$E_6 = E_{b_6} + C|D_6|^2 \sin^2 \theta, \quad (\text{A8})$$

which is the uncoupled behavior exhibited by the LE in Fig. 6 represented by crossed dashed lines.

6. Coupled bright excitons

We now consider that the two excitons E_3 and E_6 are coupled. In this situation H_{ij}^{SR} and V_{ij}^{LR} become 2×2 matrices, and their substitution in Eq. (A5) results in an eigenvalue problem with solutions:

$$E_{\pm} = \frac{E_{b_3} + E_{b_6} + C|D_3|^2(a^2 + b^2) \pm \sqrt{(C|D_3|^2(a^2 + b^2) + E_{b_3} + E_{b_6})^2 - 4[C|D_3|^2(E_{b_6}a^2 + E_{b_3}b^2) + E_{b_3}E_{b_6}]}}{2}, \quad (\text{A9})$$

where $a = \cos \theta$ and $b = \frac{D_6}{D_3} \sin \theta$. In Fig. 6 the coupled exciton E_+ is represented by the magenta curve, whereas the other coupled exciton E_- is depicted by the green curve. The fact that the solutions of Eq. (A9) do not perfectly represent the behavior obtained by BSE is because we are only considering the first bright exciton for the in-plane and out-of-plane directions and therefore do not consider

the effect of other less coupled bright excitons at higher energies.

7. Full list of computational details

In this Appendix we show in Tables IV, V, and VI the parameters used to carry out the DFT, GW, and BSE calculations for the bulk and monolayer BiI₃.

- [1] S. A. Moskalenko and D. W. Snoke, *Bose-Einstein Condensation of Excitons and Biexcitons: And Coherent Nonlinear Optics with Excitons* (Cambridge University Press, Cambridge, UK, 2000).
- [2] Y. Morita, K. Yoshioka, and M. Kuwata-Gonokami, Observation of Bose-Einstein condensates of excitons in a bulk semiconductor, *Nat. Commun.* **13**, 5388 (2022).
- [3] E. Perfetto and G. Stefanucci, Floquet topological phase of nondriven p -wave nonequilibrium excitonic insulators, *Phys. Rev. Lett.* **125**, 106401 (2020).
- [4] E. Perfetto, D. Sangalli, A. Marini, and G. Stefanucci, Pump-driven normal-to-excitonic insulator transition: Josephson oscillations and signatures of BEC-BCS crossover in time-resolved ARPES, *Phys. Rev. Mater.* **3**, 124601 (2019).
- [5] A. Chernikov, C. Ruppert, H. M. Hill, A. F. Rigosi, and T. F. Heinz, Population inversion and giant bandgap renormalization in atomically thin WS₂ layers, *Nat. Photon.* **9**, 466 (2015).
- [6] G. Wang, A. Chernikov, M. M. Glazov, T. F. Heinz, X. Marie, T. Amand, and B. Urbaszek, Colloquium: Excitons in atomically thin transition metal dichalcogenides, *Rev. Mod. Phys.* **90**, 021001 (2018).
- [7] T. Mueller and E. Malic, Exciton physics and device application of two-dimensional transition metal dichalcogenide semiconductors, *npj 2D Mater. Appl.* **2**, 29 (2018).
- [8] M. M. Ugeda, A. J. Bradley, S.-F. Shi, F. H. da Jornada, Y. Zhang, D. Y. Qiu, W. Ruan, S.-K. Mo, Z. Hussain, Z.-X. Shen, F. Wang, S. G. Louie, and M. F. Crommie, Giant bandgap renormalization and excitonic effects in a monolayer transition metal dichalcogenide semiconductor, *Nat. Mater.* **13**, 1091 (2014).
- [9] Q. H. Wang, K. Kalantar-Zadeh, A. Kis, J. N. Coleman, and M. S. Strano, Electronics and optoelectronics of two-dimensional transition metal dichalcogenides, *Nat. Nanotechnol.* **7**, 699 (2012).
- [10] J. R. Schaibley, H. Yu, G. Clark, P. Rivera, J. S. Ross, K. L. Seyler, W. Yao, and X. Xu, Valleytronics in 2D materials, *Nat. Rev. Mater.* **1**, 16055 (2016).
- [11] F. Tagarelli, E. Lopriore, D. Erckensten, R. Perea-Causín, S. Brem, J. Hagel, Z. Sun, G. Pasquale, K. Watanabe, T. Taniguchi, E. Malic, and A. Kis, Electrical control of hybrid exciton transport in a van der Waals heterostructure, *Nat. Photon.* **17**, 615 (2023).
- [12] G. Pasquale, Z. Sun, K. Čerņevičs, R. Perea-Causin, F. Tagarelli, K. Watanabe, T. Taniguchi, E. Malic, O. V. Yazyev, and A. Kis, Flat-band-induced many-body interactions and exciton complexes in a layered semiconductor, *Nano Lett.* **22**, 8883 (2022).
- [13] A. Ciarrocchi, F. Tagarelli, A. Avsar, and A. Kis, Excitonic devices with van der Waals heterostructures: Valleytronics meets twistrionics, *Nat. Rev. Mater.* **7**, 449 (2022).
- [14] J. Madéo, M. K. L. Man, C. Sahoo, M. Campbell, V. Pareek, E. L. Wong, A. Al-Mahboob, N. S. Chan, A. Karmakar, B. M. K. Mariserla, X. Li, T. F. Heinz, T. Cao, and K. M. Dani, Directly visualizing the momentum-forbidden dark excitons and their dynamics in atomically thin semiconductors, *Science* **370**, 1199 (2020).
- [15] D. Schmitt, J. P. Bange, W. Bennecke, A. AlMutairi, G. Meneghini, K. Watanabe, T. Taniguchi, D. Steil, D. R. Luke, R. T. Weitz, S. Steil, G. S. M. Jansen, S. Brem, E. Malic, S. Hofmann, M. Reutzler, and S. Mathias, Formation of moiré interlayer excitons in space and time, *Nature (London)* **608**, 499 (2022).
- [16] E. Torun, H. P. C. Miranda, A. Molina-Sánchez, and L. Wirtz, Interlayer and intralayer excitons in MoS₂/WS₂ and MoSe₂/WSe₂ heterobilayers, *Phys. Rev. B* **97**, 245427 (2018).
- [17] W. Lee, Y. Lin, L.-S. Lu, W.-C. Chueh, M. Liu, X. Li, W.-H. Chang, R. A. Kaindl, and C.-K. Shih, Time-resolved ARPES determination of a quasi-particle band gap and hot electron dynamics in monolayer MoS₂, *Nano Lett.* **21**, 7363 (2021).
- [18] M. K. L. Man, J. Madéo, C. Sahoo, K. Xie, M. Campbell, V. Pareek, A. Karmakar, E. L. Wong, A. Al-Mahboob, N. S. Chan, D. R. Bacon, X. Zhu, M. M. M. Abdelrasoul, X. Li, T. F. Heinz, F. H. d. Jornada, T. Cao, and K. M. Dani, Experimental measurement of the intrinsic excitonic wave function, *Sci. Adv.* **7**, eabg0192 (2021).
- [19] A. Raja, A. Chaves, J. Yu, G. Arefe, H. M. Hill, A. F. Rigosi, T. C. Berkelbach, P. Nagler, C. Schüller, T. Korn, C. Nuckolls, J. Hone, L. E. Brus, T. F. Heinz, D. R. Reichman, and A. Chernikov, Coulomb engineering of the bandgap and excitons in two-dimensional materials, *Nat. Commun.* **8**, 15251 (2017).
- [20] R. E. Brandt, R. C. Kurchin, R. L. Z. Hoye, J. R. Poindexter, M. W. B. Wilson, S. Sulekar, F. Lenahan, P. X. T. Yen, V. Stevanović, J. C. Nino, M. G. Bawendi, and T. Buonassisi, Investigation of bismuth triiodide (BiI₃) for photovoltaic applications, *J. Phys. Chem. Lett.* **6**, 4297 (2015).
- [21] A. J. Lehner, H. Wang, D. H. Fabini, C. D. Liman, C.-A. Hébert, E. E. Perry, M. Wang, G. C. Bazan, M. L. Chabinc, and R. Seshadri, Electronic structure and photovoltaic application of BiI₃, *Appl. Phys. Lett.* **107**, 131109 (2015).
- [22] M. Matsumoto, K. Hitomi, T. Shoji, and Y. Hiratate, Bismuth tri-iodide crystal for nuclear radiation detectors, *IEEE Trans. Nucl. Sci.* **49**, 2517 (2002).
- [23] F. E. Rosztoczy and D. Cubicciotti, The bismuth iodide-iodine phase diagram I, *J. Phys. Chem.* **69**, 124 (1965).
- [24] Y. Kaifu, Excitons in layered BiI₃ single crystals, *J. Lumin.* **42**, 61 (1988).
- [25] S. Mor, V. Gosetti, A. Molina-Sánchez, D. Sangalli, S. Achilli, V. F. Agekyan, P. Franceschini, C. Giannetti, L. Sangaletti, and S. Pagliara, Photoinduced modulation of the excitonic resonance via coupling with coherent phonons in a layered semiconductor, *Phys. Rev. Res.* **3**, 043175 (2021).
- [26] D. Mu, W. Zhou, Y. Liu, J. Li, M. Yang, J. Zhuang, Y. Du, and J. Zhong, Resolving the intrinsic bandgap and edge effect of BiI₃ film epitaxially grown on graphene, *Mater. Today Phys.* **20**, 100454 (2021).
- [27] S. Takeyama, K. Watanabe, and T. Komatsu, Thin-film single-crystal growth of BiI₃ by a hot wall technique, *Jpn. J. Appl. Phys.* **29**, 710 (1990).
- [28] A. Garg, M. Tomar, and V. Gupta, Synthesis and characterisation of thin films of bismuth triiodide for semiconductor radiation detectors, in *Conference Papers in Science* (Hindawi Publishing Corporation, Dehradun, India, 2014), Vol. 2014.
- [29] F. Ma, M. Zhou, Y. Jiao, G. Gao, Y. Gu, A. Bilic, Z. Chen, and A. Du, Single layer bismuth iodide: Computational exploration of structural, electrical, mechanical and optical properties, *Sci. Rep.* **5**, 1 (2015).
- [30] E. C. Ahn, 2D materials for spintronic devices, *npj 2D Mater. Appl.* **4**, 17 (2020).
- [31] W.-Z. Xiao, G. Xiao, Z.-J. Wang, and L.-L. Wang, Large exciton binding energy, superior mechanical flexibility, and

- ultra-low lattice thermal conductivity in BiI₃ monolayer, *J. Phys.: Condens. Matter* **34**, 055302 (2022).
- [32] P. Giannozzi, S. Baroni, N. Bonini, M. Calandra, R. Car, C. Cavazzoni, D. Ceresoli, G. L. Chiarotti, M. Cococcioni, I. Dabo, A. D. Corso, S. de Gironcoli, S. Fabris, G. Fratesi, R. Gebauer, U. Gerstmann, C. Gougoussis, A. Kokalj, M. Lazzeri, L. Martin-Samos *et al.*, QUANTUM ESPRESSO: A modular and open-source software project for quantum simulations of materials, *J. Phys.: Condens. Matter* **21**, 395502 (2009).
- [33] P. Giannozzi, O. Andreussi, T. Brumme, O. Bunau, M. B. Nardelli, M. Calandra, R. Car, C. Cavazzoni, D. Ceresoli, M. Cococcioni, N. Colonna, I. Carnimeo, A. D. Corso, S. de Gironcoli, P. Delugas, R. A. DiStasio, A. Ferretti, A. Floris, G. Fratesi, G. Fugallo *et al.*, Advanced capabilities for materials modelling with QUANTUM ESPRESSO, *J. Phys.: Condens. Matter* **29**, 465901 (2017).
- [34] P. Giannozzi, O. Baseggio, P. Bonfá, D. Brunato, R. Car, I. Carnimeo, C. Cavazzoni, S. de Gironcoli, P. Delugas, F. Ferrari Ruffino, A. Ferretti, N. Marzari, I. Timrov, A. Urru, and S. Baroni, QUANTUM ESPRESSO toward the exascale, *J. Chem. Phys.* **152**, 154105 (2020).
- [35] J. P. Perdew, K. Burke, and M. Ernzerhof, Generalized gradient approximation made simple, *Phys. Rev. Lett.* **77**, 3865 (1996).
- [36] A. Tkatchenko and M. Scheffler, Accurate molecular van der Waals interactions from ground-state electron density and free-atom reference data, *Phys. Rev. Lett.* **102**, 073005 (2009).
- [37] M. van Setten, M. Giantomassi, E. Bousquet, M. Verstraete, D. Hamann, X. Gonze, and G.-M. Rignanese, The PSEUDO-DODOJO: Training and grading a 85 element optimized norm-conserving pseudopotential table, *Comput. Phys. Commun.* **226**, 39 (2018).
- [38] P. Scherpelz, M. Govoni, I. Hamada, and G. Galli, Implementation and validation of fully relativistic GW calculations: Spin-orbit coupling in molecules, nanocrystals, and solids, *J. Chem. Theory Comput.* **12**, 3523 (2016).
- [39] F. Giustino, *Materials Modelling Using Density Functional Theory: Properties and Predictions* (Oxford University Press, Oxford, UK, 2014).
- [40] D. Nason and L. Keller, The growth and crystallography of bismuth tri-iodide crystals grown by vapor transport, *J. Cryst. Growth* **156**, 221 (1995).
- [41] H. J. Monkhorst and J. D. Pack, Special points for Brillouin-zone integrations, *Phys. Rev. B* **13**, 5188 (1976).
- [42] L. Reining, The GW approximation: Content, successes and limitations, *WIREs Comput. Mol. Sci.* **8**, e1344 (2018).
- [43] G. Onida, L. Reining, and A. Rubio, Electronic excitations: Density-functional versus many-body Green's-function approaches, *Rev. Mod. Phys.* **74**, 601 (2002).
- [44] G. Strinati, Application of the Green's functions method to the study of the optical properties of semiconductors, *La Rivista del Nuovo Cimento* **11**, 1 (1988).
- [45] A. Marini, C. Hogan, M. Grüning, and D. Varsano, YAMBO: An ab initio tool for excited state calculations, *Comput. Phys. Commun.* **180**, 1392 (2009).
- [46] D. Sangalli, A. Ferretti, H. Miranda, C. Attaccalite, I. Marri, E. Cannuccia, P. Melo, M. Marsili, F. Paleari, A. Marrazzo, G. Prandini, P. Bonfá, M. O. Atambo, F. Affinito, M. Palummo, A. Molina-Sánchez, C. Hogan, M. Grüning, D. Varsano, and A. Marini, Many-body perturbation theory calculations using the YAMBO code, *J. Phys.: Condens. Matter* **31**, 325902 (2019).
- [47] M. Marsili, A. Molina-Sánchez, M. Palummo, D. Sangalli, and A. Marini, Spinorial formulation of the GW-BSE equations and spin properties of excitons in two-dimensional transition metal dichalcogenides, *Phys. Rev. B* **103**, 155152 (2021).
- [48] A. Stan, N. E. Dahlen, and R. van Leeuwen, Levels of self-consistency in the GW approximation, *J. Chem. Phys.* **130**, 114105 (2009).
- [49] H. N. Rojas, R. W. Godby, and R. J. Needs, Space-time method for ab initio calculations of self-energies and dielectric response functions of solids, *Phys. Rev. Lett.* **74**, 1827 (1995).
- [50] D. Bohm and D. Pines, A collective description of electron interactions. III. Coulomb interactions in a degenerate electron gas, *Phys. Rev.* **92**, 609 (1953).
- [51] A. Guandalini, P. D'Amico, A. Ferretti, and D. Varsano, Efficient GW calculations in two dimensional materials through a stochastic integration of the screened potential, *npj Comput. Mater.* **9**, 44 (2023).
- [52] F. Bruneval and X. Gonze, Accurate GW self-energies in a plane-wave basis using only a few empty states: Towards large systems, *Phys. Rev. B* **78**, 085125 (2008).
- [53] M. Ruck, Darstellung und kristallstruktur von fehlordnungs-freiem bismuttriodid, *Z. Kristallogr. Cryst. Mater.* **210**, 650 (1995).
- [54] H. Yorikawa and S. Muramatsu, Theoretical study of crystal and electronic structures of BiI₃, *J. Phys.: Condens. Matter* **20**, 325220 (2008).
- [55] Z. Zhou, A. Li, F. Wu, C. Huang, and E. Kan, Two-dimensional ferroelectricity in a single-atom adsorbed BiI₃ monolayer, *J. Phys. Chem. C* **127**, 3898 (2023).
- [56] B. Huang, G. Clark, E. Navarro-Moratalla, D. R. Klein, R. Cheng, K. L. Seyler, D. Zhong, E. Schmidgall, M. A. McGuire, D. H. Cobden *et al.*, Layer-dependent ferromagnetism in a van der Waals crystal down to the monolayer limit, *Nature (London)* **546**, 270 (2017).
- [57] N. J. Podraza, W. Qiu, B. B. Hinojosa, H. Xu, M. A. Motyka, S. R. Phillpot, J. E. Baciai, S. Trolrier-McKinstry, and J. C. Nino, Band gap and structure of single crystal BiI₃: Resolving discrepancies in literature, *J. Appl. Phys.* **114**, 033110 (2013).
- [58] K. F. Mak, C. Lee, J. Hone, J. Shan, and T. F. Heinz, Atomically thin MoS₂: A new direct-gap semiconductor, *Phys. Rev. Lett.* **105**, 136805 (2010).
- [59] A. Molina-Sánchez, K. Hummer, and L. Wirtz, Vibrational and optical properties of MoS₂: From monolayer to bulk, *Surf. Sci. Rep.* **70**, 554 (2015).
- [60] A. Chernikov, T. C. Berkelbach, H. M. Hill, A. Rigosi, Y. Li, B. Aslan, D. R. Reichman, M. S. Hybertsen, and T. F. Heinz, Exciton binding energy and nonhydrogenic Rydberg series in monolayer WS₂, *Phys. Rev. Lett.* **113**, 076802 (2014).
- [61] A. Molina-Sánchez, G. Catarina, D. Sangalli, and J. Fernández-Rossier, Magneto-optical response of chromium trihalide monolayers: Chemical trends, *J. Mater. Chem. C* **8**, 8856 (2020).
- [62] T. Komatsu and Y. Kaifu, Optical properties of bismuth tri-iodide single crystals. I. Interband Transitions, *J. Phys. Soc. Jpn.* **40**, 1062 (1976).
- [63] E. Jung, J. C. Park, Y.-S. Seo, J.-H. Kim, J. Hwang, and Y. H. Lee, Unusually large exciton binding energy in multilayered 2H-MoTe₂, *Sci. Rep.* **12**, 4543 (2022).
- [64] C. Robert, R. Picard, D. Lagarde, G. Wang, J. P. Echeverry, F. Cadiz, P. Renucci, A. Högele, T. Amand, X. Marie, I. C.

- Gerber, and B. Urbaszek, Excitonic properties of semiconducting monolayer and bilayer MoTe₂, *Phys. Rev. B* **94**, 155425 (2016).
- [65] A. Arora, M. Drüppel, R. Schmidt, T. Deilmann, R. Schneider, M. R. Molas, P. Marauhn, S. Michaelis de Vasconcellos, M. Potemski, M. Rohlfing *et al.*, Interlayer excitons in a bulk van der Waals semiconductor, *Nat. Commun.* **8**, 639 (2017).
- [66] S. Haastrup, M. Strange, M. Pandey, T. Deilmann, P. S. Schmidt, N. F. Hinsche, M. N. Gjerding, D. Torelli, P. M. Larsen, A. C. Riis-Jensen, J. Gath, K. W. Jacobsen, J. J. Mortensen, T. Olsen, and K. S. Thygesen, The computational 2D materials database: High-throughput modeling and discovery of atomically thin crystals, *2D Mater.* **5**, 042002 (2018).
- [67] D. Sangalli, Excitons and carriers in transient absorption and time-resolved ARPES spectroscopy: An *ab initio* approach, *Phys. Rev. Mater.* **5**, 083803 (2021).
- [68] M. Dvorak, S.-H. Wei, and Z. Wu, Origin of the variation of exciton binding energy in semiconductors, *Phys. Rev. Lett.* **110**, 016402 (2013).
- [69] L. C. Andreani, F. Bassani, and A. Quattropani, Longitudinal-transverse splitting in Wannier excitons and polariton states, *II Nuovo Cimento D* **10**, 1473 (1988).
- [70] P. Y. Yu and M. Cardona, *Fundamentals of Semiconductors: Physics and Materials Properties* (Springer Berlin Heidelberg, 2010).
- [71] R. Del Sole and E. Fiorino, Macroscopic dielectric tensor at crystal surfaces, *Phys. Rev. B* **29**, 4631 (1984).
- [72] D. Y. Qiu, G. Cohen, D. Novichkova, and S. Refaely-Abramson, Signatures of dimensionality and symmetry in exciton band structure: Consequences for exciton dynamics and transport, *Nano Lett.* **21**, 7644 (2021).
- [73] To prove this, it is enough to rotate $\langle i|v^{c,LR}(\mathbf{q})|j\rangle$ in the excitonic space.
- [74] V. M. Agranovich and V. Ginzburg, *Crystal Optics with Spatial Dispersion, and Excitons* (Springer Science & Business Media, New York, 1984).
- [75] P. Cudazzo, L. Sponza, C. Giorgetti, L. Reining, F. Sottile, and M. Gatti, Exciton band structure in two-dimensional materials, *Phys. Rev. Lett.* **116**, 066803 (2016).
- [76] R. Hambach, Theory and *ab-initio* calculations of collective excitations in nanostructures: Towards spatially-resolved EELS, Ph.D. thesis, École Polytechnique, 2010.
- [77] Our BSE calculations are restricted to ϵ_L in this work. At finite momentum in 2D, the long-range exchange still gives two branches with two different dispersions, as already discussed in the literature. One parabolic with dipole perpendicular to the \mathbf{q} direction (TE branch), and one linear, with dipole parallel to the \mathbf{q} direction (LE branch), e.g., there is L-T splitting at finite momentum in 2D. The TE branch could be detected by measuring $\epsilon_T(\mathbf{q}, \omega) \neq \epsilon_L(\mathbf{q}, \omega)$ at $\mathbf{q} \neq 0$.